RESEARCH

In-situ synthesis of NiCo$_2$S$_4$@graphene composite for high-performance supercapacitor

Xiaojun Xu[1] · HuiZhong Xu[1] · Qiannan Zhou[1,2] · Weifeng Liu[1] · Jie Gao[1] · Ziqiushui Zhuang[1] · Xin Zhou[1] · Wei Li[1]

Abstract

Binary transition metal sulfides have garnered widespread concentration result from their superior electrical conductivity and outstanding capacitance. However, their poor cycling stability hinders their applications in energy storage devices. The objective of this study is to devise and prepare graphene and NiCo$_2$S$_4$ composite (NiCo$_2$S$_4$@graphene) using a simple one-step hydrothermal modality. Graphene is used as a conductive substrate, and NiCo$_2$S$_4$ nanoparticles are formed in situ and homogeneously anchored on graphene nanosheets through C-S-C covalent bonds. For example, the NiCo$_2$S$_4$@graphene composite has a high specific capacitance of 918.0 C g^{-1} at a current density of 1 A g^{-1} and enhanced cycling stability (90.1% after 6000 cycles). In addition, the asymmetric supercapacitor was fabricated with NiCo$_2$S$_4$@graphene as the positive electrode and graphene (GR) as the negative electrode, and the device provided a maximum energy density of 49.8 Wh kg^{-1} at a power density of 845.3 Wh kg^{-1}. Besides, the capacitance retention rate was as high as 92.0% after 1000 cycles. The superior electrochemical properties of the NiCo$_2$S$_4$@graphene material verified its huge potential for realistic applications.

Keywords NiCo$_2$S$_4$ · Graphene · Supercapacitors · Covalent bonds · Synergistic effect

Introduction

The pollution and non-renewability of conventional oil resources have been obstacles to sustainable development for humans. Accordingly, there is much interest in developing environmental benignity and low-cost and clean renewable energy sources [1, 2]. Scientists and researchers have been focusing on developing and studying electrochemical energy storage technologies such as lithium-ion batteries (LIBs) [3, 4], sodium-ion batteries (SIBs) [5, 6], and supercapacitors (SCs) [7, 8]. Supercapacitors are new energy devices that combines the characteristics of conventional capacitors with the energy storage properties of batteries.

Supercapacitors offer several advantages, including good safety, high power density, rapid charging and discharging rates, and long cycle life [9, 10]. Supercapacitors can be categorized into electric double-layer capacitors (EDLCs) and pseudocapacitors based on their operating principles [11]. The electrical double-layer capacitors store energy primarily through the interfacial double layer formed between the electrodes and the electrolyte [12]. An critical characteristic of this process is that no transfer of charge occurring at the interface between the electrode and electrolyte. In other words, it is a non-Faraday process [13]. Pseudocapacitors rely heavily on the Faraday process to store charges, which involves rapid and reversible oxidation and reduction reactions on or around the superficies of the active material [14]. Among the above two mechanisms, the bilayer capacitor usually shows higher rate performance, and the pseudocapacitor exhibits higher capacitance performance but poorer rate performance and cycling stability. Those with the same positive and negative electrode materials are known as symmetric supercapacitors, while those with different ones are known as asymmetric supercapacitors (ASCs) [15]. In the past several years, supercapacitors have gained widespread concern due to the aforementioned advantages. Gonçalves et al. assembled supercapacitors based on trimetallic oxides

✉ Wei Li
02075@qust.edu.cn

1 Engineering Research Center of High Performance Polymer and Molding Technology, Ministry of Education, Qingdao University of Science and Technology, Qingdao 266042, People's Republic of China

2 Beijing Key Laboratory of Environmental Science and Engineering, School of Materials Science & Engineering, Beijing Institute of Technology, Beijing 100081, People's Republic of China

by (a) heteroatom doping, (b) hierarchical nanostructuring, and (c) combination with other suitable materials to prepare nanocomposites [16]. Mariappan and colleagues prepared the stand-alone carbyne (SAC) film by dehydrohalogenation on the porous polyvinylidene fluoride (PVDF) mat [17].

The performance of supercapacitors is primarily influenced by the electrode materials, which mostly include carbon materials, conductive polymers, and transition metal compounds [18]. Among them, transition metal compounds (TMCs) are capable of storing charges rapidly through Faraday reaction, with large energy storage capacity and electrical conductivity, as well as environmental friendliness [19–21]. And transition metal sulfides (TMSs) have been widely recognized due to their higher theoretical capacity and electrical conductivity, as well as more easily tunable morphology compared with other transition metal compounds [22–25]. Compared with mono-metal sulfides, such as CoS_2 [26], NiS_2 [27], MoS_2 [28], and MnS [29], bimetallic sulfides, such as $CoMoS_4$ [30] and $NiCo_2S_4$ [31] have better electrical conductivity and richer redox reactions, which can provide higher specific capacitance and exhibit better electrochemical properties. Therefore, bimetallic sulfides are regarded as a new research hotspot in supercapacitors [32].

Among the various TMSs, $NiCo_2S_4$-based materials have a high theoretical specific capacitance and are therefore considered by researchers as ideal electrode materials for supercapacitors. The current studies report that different nanostructures of $NiCo_2S_4$ materials have been successfully designed, such as nanoneedles [32], nanosheets [33], nanoparticles [34], and nanospheres [35]. However, among the many $NiCo_2S_4$ morphologies, fewer reports on $NiCo_2S_4$ nanoparticles have been reported. For instance, Xin and colleagues reported the devise and synthesis of nanoflower-$NiCo_2S_4$ with remarkable performance (specific capacitance of 1141.0 F g^{-1} at 1 A g^{-1}) using low-cost $[CH_3NH_3][Ni(HCOO)_3]$ and $[CH_3NH_3]$ $[Co(HCOO)_3]$ as the precursor [36]. Xiang et al. Successfully reported an approach for designing and synthesizing $NiCo_2S_4$ polyhedral structures with stable structure and good performance (specific capacitance of 1298.0 F g^{-1} at 1 A g^{-1}) using $NiCo_2O_4$ as the precursor [37]. However, although NiCo2S4 materials are used as excellent battery materials, $NiCo_2S_4$ nanoparticles tend to aggregate during charging and discharging, which reduces the stability and specific capacitance of supercapacitors [38]. Moreover, the alteration in the volume of NiCo2S4 nanoparticles during cycling results in a rapid decrease in the capacity and cycling stability of the $NiCo_2S_4$ material [39]. To address these disadvantages of the NiCo2S4 material, researchers considered combining the $NiCo_2S_4$ material with a conductive substrate to improve its electrochemical properties. Typically, carbon spheres [40], graphene [41], Ni foam [42], and carbonized polymer sponges [43] are chosen as conductive substrates. For instance, Mariappan et al. used

antimonene sheets as a conductive substrate to grow nanostructures to generate antimonene/3DNi [44]. Tian et al. used CNT fiber as the primary core and in situ growth on CNT to obtain PANI/N-CNT@CNT fiber [45]. However, most of the composites of $NiCo_2S_4$ nanoparticles and carbon materials are simply mixed, and the $NiCo_2S_4$ nanoparticles cannot be tightly bonded with the carbon materials, thus easily leading to the dislodgement of $NiCo_2S_4$ nanoparticles from the carbon materials during the charging and discharging process [46, 47].

In this work, we prepared $NiCo_2S_4$@graphene composite by a simple one-step hydrothermal method, which uses graphene nanosheets as conductive substrate and immobilizes $NiCo_2S_4$ nanoparticles onto graphene nanosheets by constructing C-S-C covalent bonds. Graphene is a 2D monolayer material with a theoretical specific surface area of up to 2630 m^2 g^{-1}, which facilitates electron transport and exposes numerous adsorption sites. Therefore, it is capable of being an excellent conductive substrate for $NiCo_2S_4$ nanoparticles [48, 49]. Graphene nanosheets can avoid the agglomeration of NiCo2S4 nanoparticles to a certain extent [50]. Meanwhile, the lamellar structure of graphene nanosheets provides protection for NiCo2S4 nanoparticles, hinders the volume variation of $NiCo_2S_4$ nanoparticles during charge/discharge process, and effectively improves the cycling stability of the material. In addition, $NiCo_2S_4$ nanoparticles enter into the interlayers of graphene nanosheets, effectively reducing the agglomeration of graphene nanosheets, thereby enhancing the material's electrical conductivity [51]. Meanwhile, the construction of C-S-C covalent bonds enhance the interfacial interaction between $NiCo_2S_4$ nanoparticles and graphene, anchoring $NiCo_2S_4$ nanoparticle firmly on the graphene conducting substrate, thus improving the charge transfer of $NiCo_2S_4$@graphene composite. $NiCo_2S_4$@graphene electrodes presented a high capacitance of up to 918.0 C g^{-1} at 1 A g^{-1}, and they also demonstrate exceptional cycling stability with a capacitance retention of 90.4% even after 5000 cycles. The asymmetric supercapacitor was assembled with $NiCo_2S_4$@graphene as the positive electrode and graphene (GR) as the negative electrode. Such device exhibited a remarkable energy density of 49.8 Wh kg^{-1} at a power density of 845.3 Wh kg^{-1} and a remarkable capacitance retention rate of 92.0% after 1000 cycles. With the $NiCo_2S_4$@graphene composite exhibit good cycling stability and capacitance performance, their great potential for supercapacitors applications is verified.

Experimental section

Synthesis of $NiCo_2S_4$@graphene composite

$NiCo_2S_4$@graphene composite was synthesized by a typical one-step hydrothermal method. First, 50 mg graphene was

once brought to a combination of 40 ml deionized water and 20 ml anhydrous ethanol to gain a homogeneous suspension by means of sonication. Then, 1 mmol $Ni(NO_3)_2 \cdot 6H_2O$, 2 mmol $Co(NO_3)_2 \cdot 6H_2O$, and 7 mmol thiourea were added to the above suspension and stirred at room temperature for 1 h to acquire a homogeneous mixture. The combination was then transferred into a Teflon-lined stainless steel autoclave and kept at 180 °C for 12 h. The precipitate was obtained by filtration, washed a few times with deionized water, and then, gathered after freeze-drying for 12 h.

Structural characterizations

The nanomorphology and microstructure of the samples were investigated using scanning electron microscopy (SEM, JEOL JSM-6700F) and transmission electron microscopy (TEM, JEOL JEM-2100PLUS) with energy spectroscopy (EDS). The crystal structure of the products was characterized using X-ray diffractometer (XRD, Rigaku, D/MAX/2500PC). Raman spectroscopy was carried out using a laser Raman spectrometer (Renishaw, inVia Qontor). An X-ray photoelectron spectrometer (XPS, Thermo Fisher Scientific, ESCALAB XI$^+$) was used for the valence analysis of Ni, Co, S, O, and C elements.

Electrochemical measurements

The electrochemical properties of the materials are tested by electrochemical workstation under room temperature conditions using techniques such as cyclic voltammetry (CV), galvanostatic charge-discharge (GCD), and electrochemical impedance spectroscopy (EIS). In the three-electrode measurement, $NiCo_2S_4$@graphene on nickel foam is used as the working electrode, platinum as the counter electrode, Hg/HgO electrode as the reference electrode, and 2.0 M KOH aqueous solution as electrolyte. The working electrodes were prepared by grinding the sample and carbon black into a fine powder in the ratio of 8:1 and then adding 3.0 wt% PTFE as a binder. The resulting mixture was rolled into a thin sheet and attached to nickel foam, wherein the average mass loading of the active material was 1.0–1.5 mg cm^{-2}. Then, the nickel foam containing the active material was dried in an oven at 60 °C for 12 h to obtain the working electrode. The specific capacity (C_S, C g^{-1}) of the electrode material can be calculated from the GCD curve. The calculation formula is as follows [52, 53]:

$$Cs = \frac{I\Delta t}{m} \tag{1}$$

where I (A) represents the discharge current, Δt (s) represents the discharge time, and m (g) represents the mass of the active electrode materials.

In order to assess its usefulness, asymmetric supercapacitor (ASC) was prepared with graphene as negative electrode and $NiCo_2S_4$@graphene as positive electrode. The following equations can be used to calculate the specific capacitance (C_{ASC}, F g^{-1}), the mass of the positive and negative materials, the energy density (E, Wh kg^{-1}), and the power density (P, Wh kg^{-1}) [54]:

$$C_{ASC} = \frac{I\Delta t}{M\Delta V} \tag{2}$$

$$\frac{m^+}{m^-} = \frac{\left(C_s^- \times \Delta V^-\right)}{\left(C_s^+ \times \Delta V^+\right)} \tag{3}$$

$$E = \frac{C_{ASC} \times \Delta V^2}{2 \times 3.6} \tag{4}$$

$$P = \frac{E}{\Delta t} \times 3600 \tag{5}$$

where $m^\pm$ and $C^\pm$ denote the mass and specific capacitance of the active substance at the positive (or negative) electrode, respectively; I (A), t (s), and ΔV (V) denote the discharge current, discharge time, and potential window of the ASC device, respectively [55].

Results and discussion

The process of growing $NiCo_2S_4$ nanoparticles on graphene nanosheets is proven in Fig. 1. First, graphene nanosheets were uniformly dispersed in deionized water by ultrasonication. The reaction was then carried out under hydrothermal conditions with thiourea providing the sulfur source, $Ni(NO_3)_2 \cdot 6H_2O$ providing the Ni source, and $Co(NO_3)_2 \cdot 6H_2O$ providing the Co source. Due to the strong interaction between S atoms and transition metals, $NiCo_2S_4$ nanoparticles were gradually formed and firmly dispersed on graphene nanosheets through covalent bonds C-S-C. In Fig. 2a, b, the growth of $NiCo_2S_4$ nanoparticles on graphene nanosheets is uniform and does not result in significant particle aggregation. Figures S1a and S1b show the SEM images of $NiCo_2S_4$ nanoparticles and graphene sheets, respectively. SEM images show that without the introduction of graphene sheets, the $NiCo_2S_4$ nanoparticles are clustered together, which can seriously compromise the material's electrochemical properties. Figure 2c shows the TEM image of $NiCo_2S_4$@graphene, which further illustrating that $NiCo_2S_4$ nanoparticles are uniformly distributed on graphene nanosheets. Furthermore, the curved lamellar structure of graphene nanosheets effectively suppressed the volume expansion of $NiCo_2S_4$ nanoparticles
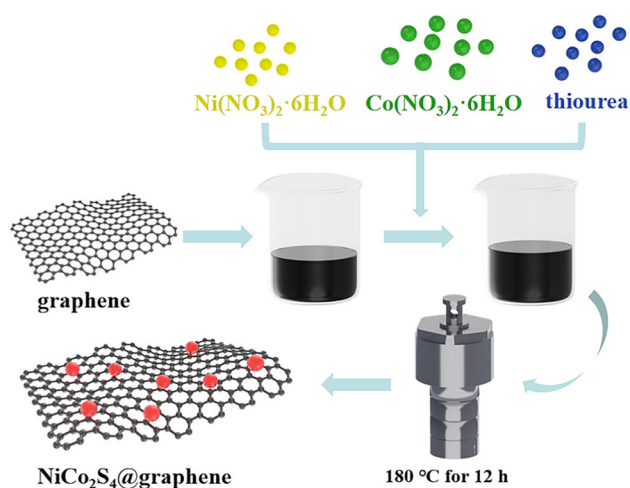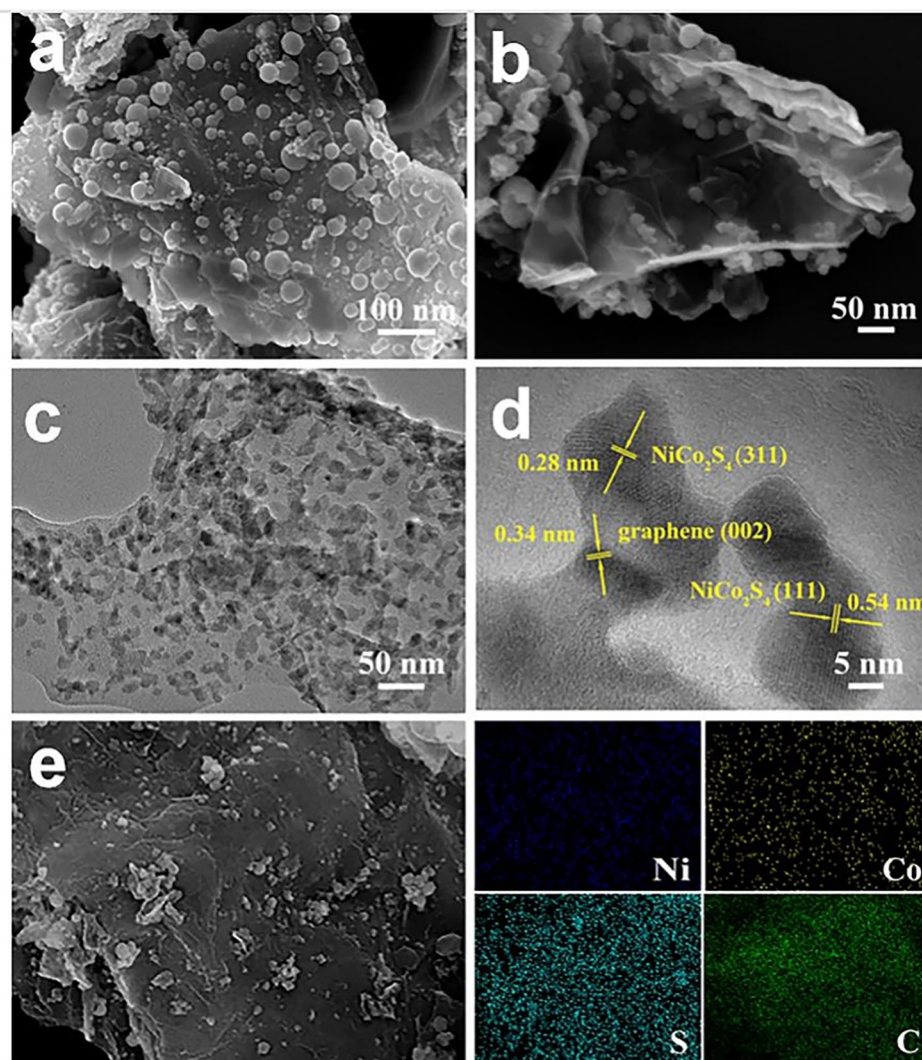
Fig. 1 Schematic of the design and synthesis of NiCo$_2$S$_4$@graphene

during the charge/discharge process. Then, the microstructure of NiCo$_2$S$_4$@graphene nanoparticles was further investigated and observed using HRTEM (Fig. 2d). The 0.28 nm and 0.54 nm lattice fringes observed in the HRTEM images are in line with the (311) and (111) planes of NiCo$_2$S$_4$, respectively, which is also supported by the XRD patterns. In addition, the lattice fringes with a pitch of 0.34 nm indexed to the (002) plane of graphene. The elemental distributions of the NiCo$_2$S$_4$@graphene and NiCo$_2$S$_4$ samples were investigated using TEM-EDS elemental mapping. Figure S1e shows the elemental distribution of NiCo$_2$S$_4$, demonstrating a uniformed distribution of elements Ni, Co, and S. Figure 2e shows the elemental distribution of NiCo$_2$S$_4$@graphene, which further demonstrates that Ni, Co, and S elements are evenly distributed on the graphene nanosheets. The graphene nanosheets possess a high specific surface area, and numerous adsorption sites can prevent the massive aggregation of NiCo$_2$S$_4$ and induce the uniform growth of NiCo$_2$S$_4$ nanoparticles on

Fig. 2 a, **b** SEM images of NiCo$_2$S$_4$@graphene. **c** TEM image of NiCo$_2$S$_4$@graphene. **d** HRTEM image of NiCo$_2$S$_4$@graphene

the graphene sheet, thus improving the material's structural stability [50].

The X-ray diffraction (XRD) patterns of $NiCo_2S_4$ and $NiCo_2S_4$@graphene are shown in Fig. 2a. The peaks of $NiCo_2S_4$ and $NiCo_2S_4$@graphene matches well with $NiCo_2S_4$ (JCPDS-20-0782) [25]. The X-ray diffraction peaks of $NiCo_2S_4$ and $NiCo_2S_4$@graphene with centers of 16.3°, 26.8°, 31.6°, 38.2°, 47.4°, 50.3°, and 55.0° can be indexed to the (111), (220), (311), (400), (422), (511), and (440) planes of $NiCo_2S_4$, respectively. These characteristic peaks confirm the successful synthesis of $NiCo_2S_4$ nanoparticles. The broad peak of $NiCo_2S_4$@graphene near 23.6° is associated with the (002) face of graphene. The results indicate that $NiCo_2S_4$@graphene composite was successfully synthesized. The Raman spectra of the $NiCo_2S_4$@graphene sample (Fig. 2b) shows two distinct peaks at 1350 cm^{-1} and 1590 cm^{-1} representing the D-band and G-band of graphene, which are usually associated with disordered and ordered graphite, respectively. By examining the intensity ratio (ID/IG) between these two bands, we can determine the level of graphene graphitization. Furthermore, the wide peak at 2700 cm^{-1} is a 2D band with a large correlation with the layer structure and stacking mode, indicating that the graphene nanosheets consist of several layers of graphene. As shown in Fig. 2c, three distinct peaks around 460, 509, and 660 cm^{-1} correlate with the F_{2g}, F_{2g}, and A_{1g} models of $NiCo_2S_4$, suggesting that $NiCo_2S_4$ was successfully introduced into graphene [55, 56].

The $NiCo_2S_4$@graphene composites were then examined using analysis by X-ray photoelectron spectroscopy (XPS) to determine their compositional composition and chemical bonding state. The presence of elements such as C, O, Ni, Co, and S in the $NiCo_2S_4$@graphene composite as shown in the full measurement spectrum of XPS in Fig. S2a. In the Ni 2p spectrum (Fig. 3e), it can be observed that in addition to the two shake-up satellites at 861.9 and 880.5 eV (considered as "Sat."), the peaks at 873.9 and 856.4 eV are related to Ni^{3+}, and the peaks at 871.5 and 854.2 eV correspond to Ni^{2+}, indicating coexistence of Ni^{3+} and Ni^{2+}. Similar to Ni 2p, except for two shake-up satellites at 786.7 and 803.3 eV, the 2p spectrum of Co (Fig. 3f) shows four peaks: the peaks are located at 778.9 and 797.2eV, respectively, corresponding to Co^{3+}; while the peaks at 781.6 and 798.9 eV indexed to Co^{2+}, suggesting the simultaneous presence of Co^{2+} and Co^{3+}. Figure S2a shows the S 2p spectrum, where the peaks at the binding energies of 161.7 and 162.8 eV are indexed as S $2p_{3/2}$ and S $2p_{1/2}$, respectively, indicating that the prepared $NiCo_2S_4$ material consists of metal-sulfur bonds. The peak at 164.3 eV is associated with an aromatic C-S-C covalent bonds, which indicates the successful construction of a C-S-C covalent bonds that can firmly anchor the $NiCo_2S_4$ nanoparticles to the graphene nanosheets and prevent the $NiCo_2S_4$ nanoparticles from falling off during cycling. The high-resolution C 1s spectrum of $NiCo_2S_4$@graphene (Fig. S2b) yields four major peaks located at 284.6, 285,0, 286.1, and 290.1 eV, attributing to C=C/C-C, C-S, C-O, and O-C=O, respectively.
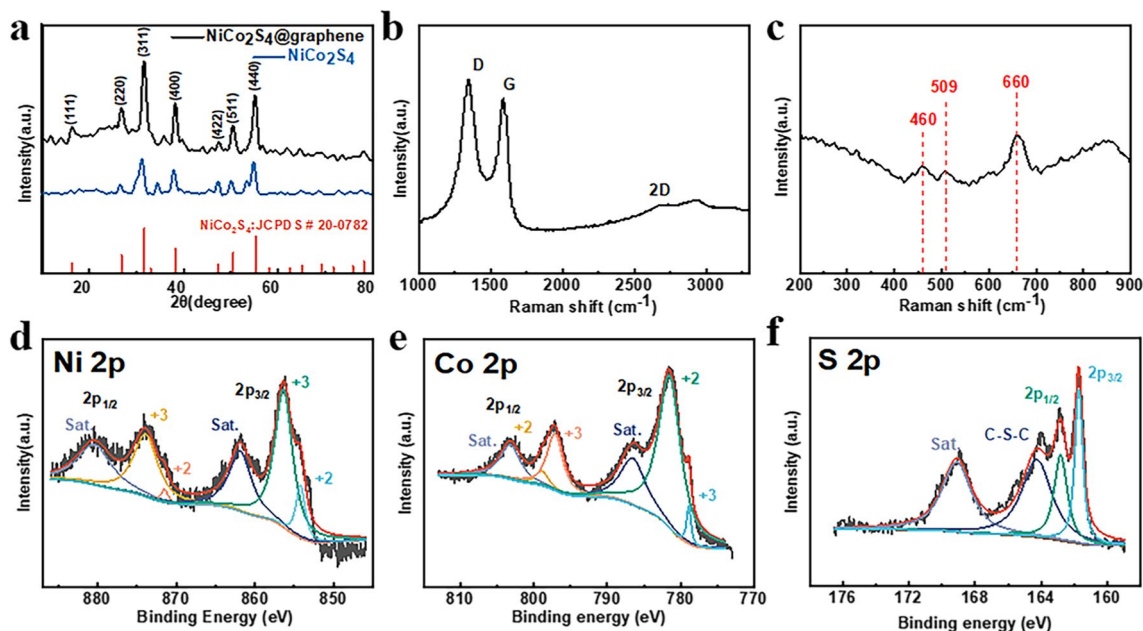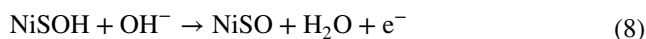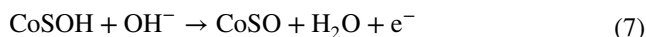

Fig. 3 a XRD patterns of $NiCo_2S_4$ and $NiCo_2S_4$@graphene; Raman spectra of $NiCo_2S_4$@graphene within different ranges: b 1000–3300 cm^{-1} and c 200–900 cm^{-1}; high-resolution XPS spectra of d Ni 2p, e Co 2p, and f S 2p in $NiCo_2S_4$@graphene

The electrochemical behavior of the working electrode including $NiCo_2S_4$ and $NiCo_2S_4$@graphene was studied with a three-electrode system under alkaline KOH electrolyte environment. A general method for characterizing the capacitive behavior of electrode materials is cyclic voltammetry (CV). Figure 4a shows the CV curves of $NiCo_2S_4$ and $NiCo_2S_4$@graphene materials at a scan rate of 20 mV s^{-1}. Based on the CV curves, there are well-defined redox peaks which corresponds to the presence of Faraday redox behavior [36]:

$$NiCo_2S_4 + OH^- + H_2O \rightarrow NiSOH + 2CoSOH + 2e^- \quad (6)$$

$$CoSOH + OH^- \rightarrow CoSO + H_2O + e^- \quad (7)$$

$$NiSOH + OH^- \rightarrow NiSO + H_2O + e^- \quad (8)$$

At the scan rate of 20 mV s^{-1}, the CV curve for $NiCo_2S_4$@graphene has a bigger area than that of $NiCo_2S_4$, suggesting that the incorporation of graphene provides the material with superior charge storage capacity [33]. Figure S3a displays the NiCo2S4@graphene electrode's CV curves for various scan rates. There may be a polarization effect between the electrode and electrolyte in the electrochemical process since the oxidation peak shifts slightly to a higher potential as scan rate is raised, while the reduction peak shifts slightly to a lower potential. Even at scanning rates as high as 100 mV s^{-1}, the CV curves still exhibit

obvious redox peaks, which indicates that the structure of $NiCo_2S_4$@graphene has the benefit of promoting rapid redox reactions. The geometry of the CV curves has fine symmetry, suggesting that the redox reaction of the electrode material has good reversibility. The charge storage mechanism of the $NiCo_2S_4$@graphene electrode is deeply explored using the following equation [57]:

$$i = av^b \quad (9)$$

$$\log(i) = \log(a) + b\log(v) \quad (10)$$

The b is the slope and is determined by a plot of $\log(i)$ and $\log(v)$. The value of b of 0.5 indicates that the electrochemical process is a diffusion-controlled process. The value of b of 1 denotes a surface-controlled process. When the b value is between 0.5 and 1, it indicates the coexistence of both control processes. The plots of the redox peaks for $\log(v)$ and $\log(i)$ of $NiCo_2S_4$@graphene are shown in Fig. S3b, and from the linear fit, it can be seen that the values for b of each of the redox peaks are 0.56 and 0.57, demonstrating that the charge storage of the $NiCo_2S_4$@graphene electrode is dictated by a combination of diffusion control and surface control. The capacitive contribution at a scan rate of 100 mV s^{-1} is 34.7% of the total capacity, as shown by the yellow-shaded area in Fig. S3c. Furthermore, the capacitive contribution of the $NiCo_2S_4$@graphene electrode is illustrated in Fig. S3d, covering scan rates that range from 5 to 100 mV s^{-1}. The capacitive contribution of the $NiCo_2S_4$@graphene
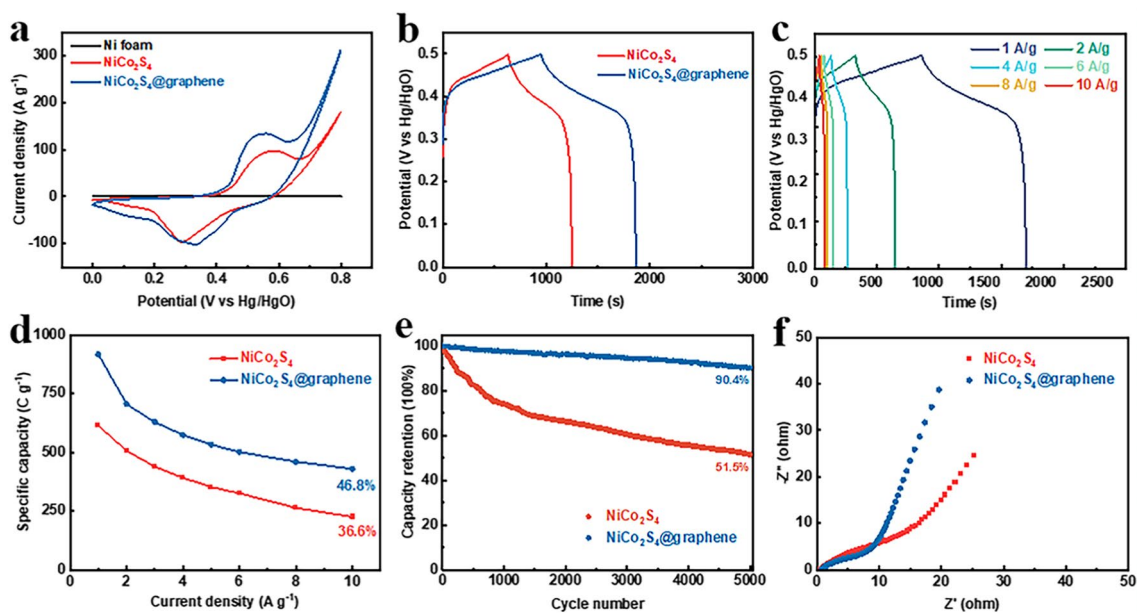

Fig. 4 **a** CV curves of $NiCo_2S_4$ and $NiCo_2S_4$@graphene at 20 mV s^{-1}; **b** GCD curves of $NiCo_2S_4$ and $NiCo_2S_4$@graphene at 1 A g^{-1}; **c** GCD curves of $NiCo_2S_4$@graphene under different current densities; **d** rate performances of $NiCo_2S_4$ and $NiCo_2S_4$@graphene at 20 mV s^{-1}; **e** cycling performance $NiCo_2S_4$ and $NiCo_2S_4$@graphene at 10 A g^{-1}. **f** EIS curve of $NiCo_2S_4$, $NiCo_2S_4$@graphene
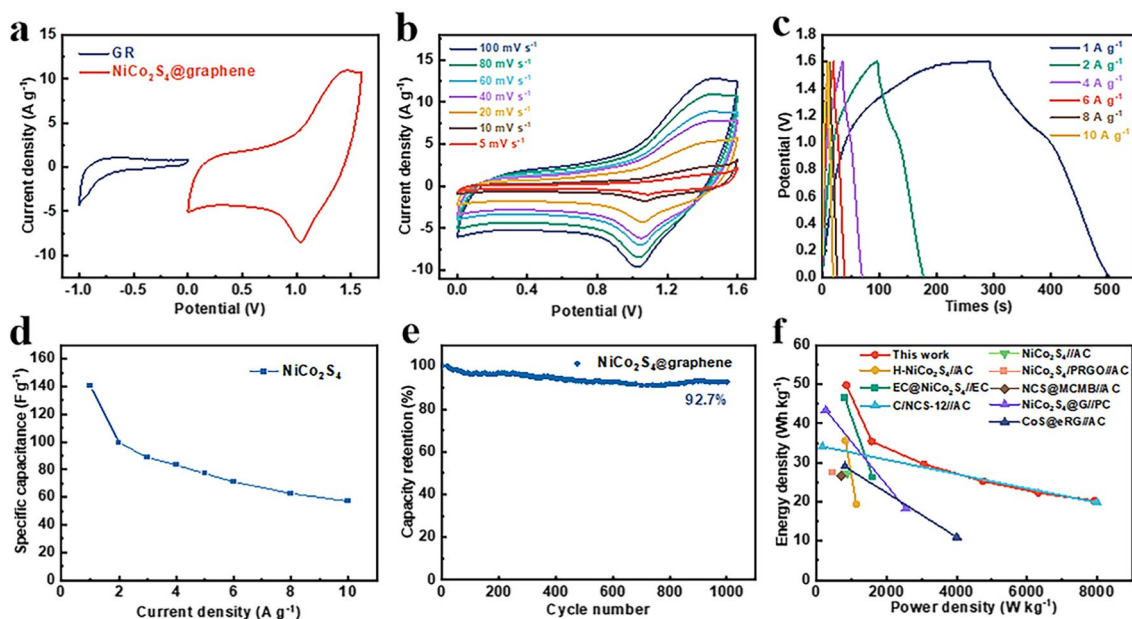
Fig. 5 **a** CV curves of NiCo$_2$S$_4$ electrode and AC electrode at scan rate of 10 mV s^{-1}. **b** CV curves of NiCo$_2$S$_4$@graphene//GR at different scan rates. **c** GCD voltage profiles at various current densities. **d** The specific capacitance values from discharge curves. **e** Cycling stability tests for NiCo$_2$S$_4$@graphene//GR at 5 A g^{-1}. **f** Ragone plot of NiCo$_2$S$_4$@graphene//GR ASC compared with other previously reported devices

electrode increases from 11.7 to 34.7% with raising scan rate. At a current density of 1 A g^{-1}, their specific capacities can be calculated from the NiCo$_2$S$_4$ and NiCo$_2$S$_4$@graphene electrodes' GCD curves (Fig. 4b) to be 614.0 and 918.0 C g^{-1}, respectively, indicating that the specific capacity could be greatly improved by adding graphene nanosheets. Figure 4c shows the GCD curves for NiCo$_2$S$_4$@graphene for a potential range from 0 to 0.5 V and at current densities of 1, 2, 4, 6, 8, and 10 A g^{-1}. The charging and discharging curves show a relatively flat slope, which corresponds to the CV curve, indicating the battery-type charge storage behavior of the NiCo$_2$S$_4$@graphene composites. The calculated specific capacities of NiCo$_2$S$_4$@graphene are 918.0, 706.0, 574.4, 501.6, 460.8, and 430.0 C g^{-1}, respectively. The NiCo$_2$S$_4$@graphene electrode's capacity increases with decreasing current density, indicating that the electrode material can be better utilized at lower current densities. The capacity of the NiCo$_2$S$_4$@graphene electrode can be maintained at around 46.8% and that of the NiCo$_2$S$_4$ electrode can be maintained around 36.6% as the current density is expanded (Fig. 4d), evidencing that the introduction of graphene improves the rate performance of NiCo$_2$S$_4$. We repeated charge/discharge testing at a constant current density of 5 A g^{-1} to examine the electrochemical stability of the electrodes in depth. After 5000 cycles, NiCo$_2$S$_4$@graphene had a specific capacity retention of 90.4%, whereas NiCo$_2$S$_4$ retained only 51.5% (Fig. 4e). The incorporation of graphene nanosheets introduced more active sites, which

enhance binding with NiCo$_2$S$_4$ and reduce the aggregation of NiCo$_2$S$_4$ material, leading to the excellent structural stability and outstanding electrochemical performance of NiCo$_2$S$_4$@ graphene. At the same time, graphene nanosheets provide protection for NiCo$_2$S$_4$ nanoparticles during charging/discharging, buffering the volume expansion of the material during charging/discharging and to enhance the material's energy storage capacity and cycling stability. Electrochemical impedance spectroscopy (EIS) measurements were conducted for NiCo$_2$S$_4$ and NiCo$_2$S$_4$@graphene composite. The slope of the Nyquist plot (Fig. 4f) in the low-frequency range represents the Warburg impedance (R_w), the intercept with the real axis at high-frequency range indicates the internal resistance (R_s), while the diameter of the semicircle reflects the interfacial charge transfer resistance (R_{ct}) [58]. Compared to pure NiCo$_2$S$_4$, NiCo$_2$S$_4$@graphene composite exhibits a higher tilt in the low-frequency range, resulting in a lower R_w for NiCo$_2$S$_4$@graphene. The intercept value of NiCo$_2$S$_4$@graphene composite is smaller than that of pure NiCo$_2$S$_4$ at high frequencies, indicating that the NiCo$_2$S$_4$@ graphene material has lower R_s. NiCo$_2$S$_4$@graphene composite has smaller semicircular diameters, which suggests that it has a smaller interfacial charge R_{ct} than pure NiCo$_2$S$_4$. Therefore, NiCo$_2$S$_4$@graphene materials have good capacitive behavior and better electrical conductivity.

To deeply investigate the practical application of the NiCo$_2$S$_4$@graphene composite, an asymmetric capacitor (ASC) was made with NiCo$_2$S$_4$@graphene as the positive

electrode, graphene (GR) as the negative electrode (noted as $NiCo_2S_4$@graphene//GR), and aqueous KOH solution as the electrolyte. Prior to this, the electrochemical properties of GR were investigated. Figure S4a shows the GCD curve of graphene at 2 A g^{-1} with a specific capacity of 128.6 C g^{-1}. According to the charge balance principle, the mass ratio of $NiCo_2S_4$@graphene to GR in the ASC was controlled to be around 1:2.7(see Eq. (1) and Eq. (3)). Figure S4b shows the EIS curves of GR. The CV curves of GR show the double-layer capacitance characteristics, indicating stable cycling properties (Fig. S4c). The stable working potential window of the electrodes was evaluated before conducting electrochemical tests. Figure 5a shows the CV curves of $NiCo_2S_4$@graphene and GR electrodes at 10 mV s^{-1} for stable potential windows of 0 to 1.6 and $-$ 1 to 0 V, respectively. Thus, the working potential window of the prepared $NiCo_2S_4$@graphene//GR ACS is 0 to 1.6 V. Figure S4d presents the CV curves of the $NiCo_2S_4$@graphene//GR ASC device for dissimilar voltage windows, in which the CV curves maintain a good geometry without obvious polarization, indicating that the ASC's stabilized operating voltage can be as high as 1.6 V. Therefore, the 0 to 1.6 V potential bias range is applied on the $NiCo_2S_4$@graphene//GR ASC. The CV curves of $NiCo_2S_4$@graphene//GR ASC at 5 to 100 mV s^{-1} are collected in Fig. 5b. The redox peak displacement of the CV curves did not change significantly as the scan rate is increased and there is no noticeable distortion in the geometry, which indicate that the ASC has outstanding reversibility and good rate property. Figure 5c displays the GCD curves of $NiCo_2S_4$@graphene//GR ASC at current densities from 1 to 10 A g^{-1}. The specific capacitance was computed by Eq. (2) to be 140.3, 99.5, 83.35, 71.18, 62.7, and 57 F g^{-1} when current densities are 1, 2, 4, 6, 8, and 10 A g^{-1}, respectively. Besides, the CV curves have apparent redox peaks, and the GCD curves have relatively flat slopes, indicating that the capacitance of ACS is the result of the combined effect of electric double-layer capacitance and pseudo-capacitance. Figure 5d demonstrates that around 41% of the capacitance is retained while the current density rises from 1 to 10 A g^{-1}. Figure 5e shows the continuous charge/discharge test for $NiCo_2S_4$@graphene//GR ASCs with a constant current density of 5A g^{-1}. After 1000 cycles, 92.7% of the capacitance of the $NiCo_2S_4$@graphene//GR ASC device is retained, demonstrating excellent cycling stability. In Fig. 5f, the Ragone plot illustrates the energy density and power density of the $NiCo_2S_4$@graphene//GR ASC device. At a power density of 845.3 Wh kg^{-1}, the device provides a maximum energy density of up to 49.8 Wh kg^{-1}. Energy density remains at 20.3 Wh kg^{-1} even after the power density is boosted to 7931.7 Wh kg^{-1}. The energy density of the $NiCo_2S_4$@graphene//GR ASC device is better

than the majority of the previously reported composites, such as H-$NiCo_2S_4$//AC [30], EC@$NiCo_2S_4$//EC [33], C/NCS-12//AC [35], $NiCo_2S_4$//AC [37], $NiCo_2S_4$/PRGO//AC [38], NCS@MCMB//AC [40], $NiCo_2S_4$@G//PC [41], and CoS@eRG//AC [59].

The synergism between $NiCo_2S_4$ and graphene is the main factor leading to the preeminent electrochemical properties of the $NiCo_2S_4$@graphene composite, specifically, as follows: (i) the bimetallic sulfide $NiCo_2S_4$ is rich in redox reactions and has a high specific capacitance; (ii) the high specific surface area of graphene can supply more adsorption sites to bind to $NiCo_2S_4$, thus greatly preventing the aggregation of $NiCo_2S_4$; (iii) the $NiCo_2S_4$@graphene composite are rich in C-S-C covalent bonds to enhance the $NiCo_2S_4$ nanoparticles interfacial bonding between the $NiCo_2S_4$ nanoparticles and graphene nanosheets, thus $NiCo_2S_4$ nanoparticles are tightly anchored on the graphene nanosheets and enhance the electrochemical kinetics; (iv) the lamellar structure of graphene nanosheets provides preservation to the $NiCo_2S_4$ nanoparticles during the charge/discharge process and buffers the volume variations of $NiCo_2S_4$ nanoparticles. At the same time, the $NiCo_2S_4$ nanoparticles can also reduce the accumulation of graphene. Thus, the cycling stability and reversibility of the material are improved, and the utilization rate of the device is enhanced.

Conclusions

In conclusion, we used a one-step hydrothermal method to construct C-S-C covalent bonds, and $NiCo_2S_4$ nanoparticles were successfully anchored on graphene nanosheets. The synergistic effect between the two reduces the buildup of $NiCo_2S_4$ nanoparticles and graphene nanosheets, and buffers the volume variations of $NiCo_2S_4$ nanoparticles. As a supercapacitor electrode, the $NiCo_2S_4$@graphene electrode has a high specific capacitance of 918.0 C g^{-1} at a current density of 1 A g^{-1} and impressive cycling stability (capacitance maintained at 90.4% after 5000 cycles). The asymmetric supercapacitor prepared based on $NiCo_2S_4$@graphene//GR electrode has a high energy density of 49.8 Wh kg^{-1} at the power density of 845.3 Wh kg^{-1}, with excellent cycling stability (92.0% capacitance retention after 1000 cycles).

Author contributions Xiaojun Xu: investigation, methodology, experiments, date analysis, and writing-original draft preparation.

Huizhong Xu: methodology and date analysis.
Qiannan Zhou: methodology and date analysis.
Weifeng Liu: methodology and date analysis.
Jie Gao: investigation and writing-reviewing.
Ziqiushui Zhuang: investigation and writing-reviewing.
Xin Zhou: investigation and writing-reviewing.

Wei Li: conceptualization, methodology, funding acquisition, project administration, review, and editing.

Data availability Data will be made available on request.

Declarations

Ethical approval Not applicable.

Competing interests The authors declare no competing interests.

References

1. Shao Y (2022) Design and mechanisms of asymmetric supercapacitors. Chem Rev 118:9233–9280. https://doi.org/10.1021/acs.chemrev.8b00252
2. Liu X, Liu CF, Xu S, Cheng T, Wang S, Lai WY, Huang W (2022) Porous organic polymers for high-performance supercapacitors. Chem Soc Rev 51:3181–3225. https://doi.org/10.1039/D2CS00065B
3. Wang C, Liu T, Yang X, Ge S, Stanley N, Rountree E, Leng Y, McCarthy B (2022) Fast charging of energy-dense lithium-ion batteries. Nature 611:485–490. https://doi.org/10.1038/S41586-022-05281-0
4. Gent WE, Busse GM, House KZ (2022) The predicted persistence of cobalt in lithium-ion batteries. Nat Energy 7:1132–1143. https://doi.org/10.1038/S41560-022-01129-Z
5. Baumann M, Häringer M, Schmidt M, Schneider L, Peters J, Bauer W, Binder J, Eil M (2022) Prospective sustainability screening of sodium-ion battery cathode materials. Adv Energy Mater 12:202202636. https://doi.org/10.1002/AENM.202202636
6. Zhao Y, Liu Q, Zhao X, Mu D, Tan G, Li L, Chen R, Wu F (2022) Structure evolution of layered transition metal oxide cathode materials for Na-ion batteries: issues, mechanism and strategies. Mater Today 62:271–295. https://doi.org/10.1016/J.MATTOD.2022.11.024
7. Giulia P (2022) Sustainable flexible supercapacitors. Nat Rev Mater 7:844. https://doi.org/10.1038/S41578-022-00508-Y
8. Huang L, Yao X, Yuan L, Yao B, Gao X, Wan J, Zhou P, Xu M, Wu J, Yu H, Hu Z, Li T, Li Y, Zhou J (2018) 4-Butylbenzenesulfonate modified polypyrrole paper for supercapacitor with exceptional cycling stability. Energy Stor Mater 12:191–196. https://doi.org/10.1016/j.ensm.2017.12.016
9. Liu X, Chen S, Xiong Z, Li K, Zhang Y (2022) Tungsten oxide-based nanomaterials for supercapacitors: mechanism, fabrication, characterization, multifunctionality, and electrochemical performance. Prog Mater Sci 130:100978. https://doi.org/10.1016/J.PMATSCI.2022.100978
10. Zhu Q, Zhao D, Cheng M, Zhou J, Owusu K, Mai L, Yu Y (2019) A New view of supercapacitors: integrated supercapacitors. Adv Energy Mater 9(36):1901081. https://doi.org/10.1002/aenm.201901081
11. Augustyn V, Simon P, Dunn B (2014) Pseudocapacitive oxide materials for high-rate electrochemical energy storage. Energ Environ Sci 7:1597–1614. https://doi.org/10.1039/c3ee44164d
12. Zhou Y, Qi H, Yang J, Bo Z, Huang F, Islam M, Lu X, Dai L, Amal R, Wang C, Han Z (2021) Two-birds-one-stone: multifunctional supercapacitors beyond traditional energy storage. Energ Environ Sci 14:1854–1896. https://doi.org/10.1039/D0EE03167D
13. Zhang C (2016) Supercapacitors: performance doping. Nat Energy 350:1508–1513. https://doi.org/10.1038/nenergy.2016.6
14. Xu T, Li Z, Wang D, Zhang M, Ai L, Chen Z, Zhang J, Zhang X, Shen L (2022) A fast proton-induced pseudocapacitive supercapacitor with high energy and power density. Adv Funct Mater 32:2107720. https://doi.org/10.1002/ADFM.202107720
15. Shao Y, El-Kady M, Sun J, Li Y, Zhang Q, Zhu M, Wang H, Dunn B, Kaner R (2018) Design and mechanisms of asymmetric supercapacitors. Chem Rev 118:9233–9280. https://doi.org/10.1021/acs.chemrev.8b00252
16. Gonçalves J, Silva M, Toma H, Angnes L, Martins P, Araki K (2020) Trimetallic oxides/hydroxides as hybrid supercapacitor electrode materials: a review. J Mater Chem A 8:10534–10570. https://doi.org/10.1039/d0ta02939d
17. Mariappan V, Krishnamoorthy K, Manoharan S, Pazhamalai P, Kim S (2021) Electrospun polymer-derived carbyne supercapacitor for alternating current line filtering. Small 17:2102971, https://doi.org/10.1002/smll.202102971
18. Wang G, Zhang L, Zhang J (2012) A review of electrode materials for electrochemical supercapacitors. Chem Soc Rev 41:797–828. https://doi.org/10.1039/c1cs15060j
19. Poudel M, Kim A, Lohani P, Yoo D, Kim H (2023) Assembling zinc cobalt hydroxide/ternary sulfides heterostructure and iron oxide nanorods on three-dimensional hollow porous carbon nanofiber as high energy density hybrid supercapacitor. J Energy Storage 60:106713. https://doi.org/10.1016/j.est.2023.106713
20. Poudel M, Lohani P, Acharya D, Kandel D, Kim A, Yoo D (2023) MOF derived hierarchical ZnNiCo-LDH on vapor solid phase grown Cu_xO nanowire array as high energy density asymmetric supercapacitors. J Energy Storage 72:108220. https://doi.org/10.1016/j.est.2023.108220
21. Poudel M, Kim A, Ramakrishan S, Logeshwaran N, Ramasamy S, Kim H, Yoo D (2022) Integrating the essence of metal organic framework-derived ZnCoTe-N-C/MoS_2 cathode and ZnCo-NPS-N-CNT as anode for high-energy density hybrid supercapacitors. Compos Part B Eng 247:110339. https://doi.org/10.1016/j.compositesb.2022.110339
22. Moosavifard SE, Mohammadi A, Darzi ME, Kariman A, Abdi MM, Karimi G (2021) A facile strategy to synthesis graphene-wrapped nanoporous copper-cobalt-selenide hollow spheres as an efficient electrode for hybrid supercapacitors. Chem Eng J 415:128662. https://doi.org/10.1016/J.CEJ.2021.128662
23. Gao Y, Zhao L (2022) Review on recent advances in nanostructured transition-metal-sulfide-based electrode materials for cathode materials of asymmetric supercapacitors. Chem Eng J 430:132745. https://doi.org/10.1016/J.CEJ.2021.132745
24. Chen H, Ma X, Shen P (2019) $NiCo_2S_4$ nanocores in-situ encapsulated in graphene sheets as anode materials for lithium-ion batteries. Chem Eng J 364:167–176. https://doi.org/10.1016/j.cej.2019.01.119
25. Chen W, Wei T, Mo L, Wu S, Li Z, Chen S, Zhang X, Hu L, Chen W (2020) CoS_2 nanosheets on carbon cloth for flexible all-solid-state supercapacitors. Chem Eng J 400:125856. https://doi.org/10.1016/j.cej.2020.125856
26. Yu X, Yu L, Wu H, Lou X (2015) Formation of nickel sulfide nanoframes from metal-organic frameworks with enhanced pseudocapacitive and electrocatalytic properties. Angew Chem 127:5421–5425. https://doi.org/10.1002/ange.201500267
27. Sun R, Liu S, Wei Q, Sheng J, Zhu S, An Q, Mai L (2017) Mesoporous NiS_2 nanospheres anode with pseudocapacitance for high-rate and long-life sodium-ion battery. Small 13:1701744. https://doi.org/10.1002/smll.201701744
28. Pazhamalai P, Krishnamoorthy K, Manoharan S, Mariappan V, Kim S (2022) Monolithic integration of MoS_2 quantum sheets on solid electrolyte for self-charging supercapacitor power cell

governed by piezo-ionic effect. Sustain Mater Technol 33:e00459. https://doi.org/10.1016/J.SUSMAT.2022.E00459

29. Zeng Q, Tian S, Liu G, Yang H, Sun X, Wang D, Huang J, Yan D, Peng S (2022) Sulfur-bridged bonds boost the conversion reaction of the flexible self-supporting MnS@MXene@CNF anode for high-rate and long-life lithium-ion batteries. ACS Appl Mater Interfaces 14:6958–6966. https://doi.org/10.1021/ACSAMI.1C24417

30. Wen Y, Peng S, Wang Z, Hao J, Qin T, Lu S, Zhang J, He D, Fan X, Cao G (2017) Facile synthesis of ultrathin NiCo$_2$S$_4$ nano-petals inspired by blooming buds for high-performance supercapacitors. J Mater Chem A 5:7144–7152. https://doi.org/10.1039/c7ta01326d

31. Zhang L, Zuo L, Fan W, Liu T (2016) NiCo$_2$S$_4$ nanosheets grown on 3D networks of nitrogen-doped graphene/carbon nanotubes: advanced anode materials for lithium-ion batteries. ChemElectroChem 3:1384–1391. https://doi.org/10.1002/celc.201600183

32. Sun T, Huang C, Shu H, Luo L, Liang Q, Chen M, Su J, Wang X (2020) Porous NiCo$_2$S$_4$ nanoneedle arrays with highly efficient electrocatalysis anchored on carbon cloths as self-supported hosts for high-loading Li-S batteries. ACS Appl Mater Interfaces 12:57975–57986. https://doi.org/10.1021/ACSAMI.0C20519

33. Liu Y, Li Z, Yao L, Chen S, Zhang P, Deng L (2019) Confined growth of NiCo$_2$S$_4$ nanosheets on carbon nanosheets derived from eggplant with enhanced performance for asymmetric supercapacitors. Chem Eng J 366:550–559. https://doi.org/10.1016/j.cej.2019.02.125

34. Ning X, Li F, Zhou Y, Miao Y, Wei C, Liu T (2017) Confined growth of uniformly dispersed NiCo$_2$S$_4$ nanoparticles on nitrogen-doped carbon nanofibers for high-performance asymmetric supercapacitors. Chem Eng J 328:599–608. https://doi.org/10.1016/j.cej.2017.07.062

35. Lu W, Yang M, Jiang X, Yu Y, Liu X, Xing Y (2020) Template-assisted synthesis of hierarchically hollow C/NiCo$_2$S$_4$ nanospheres electrode for high performance supercapacitors. Chem Eng J 382:122943. https://doi.org/10.1016/j.cej.2019.122943

36. Ma X, Guo Q, Zhang J, Su Z, Zhou S, Wei L, Li S, Yue F, Wågberg T, Hu G (2022) [CH3NH$_3$][M(HCOO)$_3$]-based 2D porous NiCo$_2$S$_4$ nanosheets for high-performance supercapacitors with high power densities. Chem Eng J 437:135337. https://doi.org/10.1016/j.cej.2022.135337

37. Xiang G, Meng Y, Qu G, Yin J, Teng B, Wei Q, Xu X (2020) Dual-functional NiCo$_2$S$_4$ polyhedral architecture with superior electrochemical performance for supercapacitors and lithium-ion batteries. Sci Bull 65:443–451. https://doi.org/10.1016/j.scib.2020.01.004

38. Zheng Y, Wang X, Zhao W, Cao X, Liu J (2018) Phytic acid-assisted synthesis of ultrafine NiCo$_2$S$_4$ nanoparticles immobilized on reduced graphene oxide as high-performance electrode for hybrid supercapacitors. Chem Eng J 333:603–612. https://doi.org/10.1016/j.cej.2017.10.008

39. Guo B, Yang T, Du W, Ma Q, Zhang L, Bao S, Li X, Chen Y, Xu M (2019) Double-walled N-doped carbon@NiCo$_2$S$_4$ hollow capsules as SeS$_2$ hosts for advanced Li-SeS$_2$ batteries. J Mater Chem A 7:12276–12282 https://doi.org/10.1039/C9TA02695A

40. Zhang Y, Zhang Y, Zhang Y, Si H, Sun L (2019) Bimetallic NiCo$_2$S$_4$ Nanoneedles anchored on mesocarbon microbeads as advanced electrodes for asymmetric supercapacitors. NanoMicro Lett 11:229–243. https://doi.org/10.1007/s40820-019-0265-1

41. Yu F, Chang Z, Yuan X, Wang F, Zhu Y, Fu L, Chen Y, Wang H, Wu Y, Li W (2018) Ultrathin NiCo$_2$S$_4$@graphene with a core-shell structure as a high performance positive electrode for hybrid supercapacitors. J Mater Chem A 6:5856–5861. https://doi.org/10.1039/c8ta00835c

42. Cui Y, Zhang J, Jin C, Liu Y, Luo W, Zheng W (2019) Ionic liquid-controlled growth of NiCo$_2$S$_4$ 3D hierarchical hollow

nanoarrow arrays on Ni foam for superior performance binder free hybrid supercapacitors. Small 15:1804318. https://doi.org/10.1002/smll.201804318

43. Li B, Song C, Rong J, Zhao J, Wang H, Yang P, Ye K, Cheng K, Zhu K, Yan J, Cao D, Wang G (2020) A new catalyst for urea oxidation: NiCo$_2$S$_4$ nanowires modified 3D carbon sponge. J Energy Chem 50:195–205. https://doi.org/10.1016/j.jechem.2019.12.018

44. Mariappan V, Krishnamoorthy K, Pazhamalai P, Natarajan S, Sahoo S, Nardekar S, Kim S (2020) Antimonene dendritic nanostructures: dual-functional material for high-performance energy storage and harvesting devices. Nano Energy 77:105248. https://doi.org/10.1016/j.nanoen.2020.105248

45. Tian J, Cui N, Chen P, Guo K, Chen X (2021) High-performance wearable supercapacitors based on PANI/N-CNT@CNT fiber with a designed hierarchical core-sheath structure. J Mater Chem A 9:20635–20644, https://doi.org/10.1039/d1ta03663g

46. Lang J, Zhang X, Liu B, Wang R, Chen J, Yan X (2018) The roles of graphene in advanced Li-ion hybrid supercapacitors. J Energy Chem 27:43–56. https://doi.org/10.1016/j.jechem.2017.11.020

47. Lu P, Jiang X, Guo W, Wang L, Zhang T, Boyjoo Y, Si W, Hou F, Liu J, Dou S, Liang J (2021) A Ni-Co sulfide nanosheet/carbon nanotube hybrid film for high-energy and high-power flexible supercapacitors. Carbon 178:355–362. https://doi.org/10.1016/j.carbon.2021.02.103

48. El-Kady M, Shao Y, Kaner R (2016) Graphene for batteries, supercapacitors and beyond. Nat Rev Mater 1:16033. https://doi.org/10.1038/natrevmats.2016.33

49. Sun Z, Wei C, Tian M, Jiang Y, Rummeli M, Yang R (2022) Plasma surface engineering of NiCo$_2$S$_4$@rGO electrocatalysts enables high-performance Li-O$_2$ batteries. ACS Appl Mater Interfaces 14:36753–36762. https://doi.org/10.1021/ACSAMI.2C10635

50. Wang P, Zhang Y, Yin Y, Fan L, Zhang N, Sun K (2018) In situ synthesis of CuCo$_2$S$_4$@N/S-doped graphene composites with pseudocapacitive properties for high-performance lithium-ion batteries. ACS Appl Mater Interfaces 10:11708–11714. https://doi.org/10.1021/acsami.8b00632

51. Brousse T, Blanger D, Long J (2015) To be or not to be pseudocapacitive. J Electrochem Soc 162:A5185–A5189. https://doi.org/10.1149/2.0201505jes

52. Laheäär A, Przygocki P, Abbas Q, Béguin F (2015) Appropriate methods for evaluating the efficiency and capacitive behavior of different types of supercapacitors. Electrochem Commun 60:21–25. https://doi.org/10.1016/j.elecom.2015.07.022

53. Mariappan V, Krishnamoorthy K, Pazhamalai P, Sahoo S, Kesavan D, Kim S (2019) Two dimensional famatinite sheets decorated on reduced graphene oxide: a novel electrode for high performance supercapacitors. J Power Sources 433:126648. https://doi.org/10.1016/j.jpowsour.2019.05.056

54. Choudhary N, Li C, Moore J, Nagaiah N, Zhai L, Jung Y, Thomas J (2017) Asymmetric supercapacitor electrodes and devices. Adv Mater 29:1605336. https://doi.org/10.1002/adma.201605336

55. Dong S, Hu P, Li X, Hong C, Zhang X, Han J (2020) NiCo$_2$S$_4$ nanosheets on 3D wood-derived carbon for microwave absorption. Chem Eng J 398:125588. https://doi.org/10.1016/j.cej.2020.125588

56. Liang X, Nie K, Ding X, Dang L, Sun J, Shi F, Xu H, Jiang R, He X, Liu Z, Lei Z (2018) Highly compressible carbon sponge supercapacitor electrode with enhanced performance by growing nickel-cobalt sulfide nanosheets. ACS Appl Mater Interfaces 10:10087–10095. https://doi.org/10.1021/acsami.7b19043

57. Wang F, Wu X, Yuan X, Liu Z, Zhang Y, Fu L, Zhu Y, Zhou Q, Wu Y, Huang W (2017) Latest advances in supercapacitors: from new electrode materials to novel device designs. Chem Soc Rev 46:6816–6854. https://doi.org/10.1039/c7cs00205j

58. Zhu T, Wang J, Ho G (2015) Self-supported yolk-shell nanocolloids towards high capacitance and excellent cycling performance. Nano Energy 18:273–282. https://doi.org/10.1016/j.nanoen.2015.10.035

59. Shi J, Li X, He G, Zhang L, Li M (2015) Electrodeposition of high-capacitance 3D CoS/graphene nanosheets on nickel foam for high-performance aqueous asymmetric supercapacitors. J Mater Chem A 3:20619–20626. https://doi.org/10.1039/c5ta04464b